ADVANCED PHOTONICS RESEARCH
Open Access
www.adpr-journal.com

Multichannel High-Efficiency Metasurfaces Based on Tri-Band Single-Cell Meta-Atoms with Independent Complex-Amplitude Modulations

Rensheng Xie, Dajun Zhang, Xiong Wang, Sensong An, Bowen Zheng, Hualiang Zhang, Guohua Zhai, Lin Li, and Jun Ding**

Achieving multitasking wavefront manipulations at multiple frequencies within a planar meta-device is pivotal for increasing data density and functionality diversity yet still challenging in integrated devices. Considering both high efficiency and compactness, herein, a high-efficiency reflective metasurface based on single-cell meta-atoms with independent complex-amplitude modulations at three distinct frequencies under the circularly polarized incidence is demonstrated, which can facilitate the formation of three mutually orthogonal channels with three distinctive functionalities. As a proof-of-concept demonstration, a tri-channel metasurface is designed and verified through both numerical simulation and experiment, where channels 1, 2, and 3 implement a dual-vortex-beam generator, a quad-focus metalens, and a meta-hologram at three different frequencies, respectively. The simulated results and the measured results have very good agreements, validating the proposed tri-band single-cell metasurface design strategy. The proposed method can open new opportunities to improve the information density and has promising prospects in image displays, communication systems, and optical storage.

1. Introduction

An ultrathin planar electromagnetic (EM) device that can achieve multiple fun ctionalities is of particular interest in compact optics and imaging systems. Metasurfaces,[1–4] as 2D analogues of metamaterials, have offered great potential to manipulate EM wavefronts through the introduction of abrupt changes in amplitude, phase, and/or polarization at a thin interface.[1,5–7] In the past decade, metasurface-based devices or meta-devices have attracted great attention, ranging from metalenses,[8–10] cloaking,[11,12] vortex beam generators,[4,13,14] hologram,[7,15–23] to nonlinear response.[3,24,25] However, due to the dispersive nature, metasurfaces usually work at one single-frequency band, i.e., achieving the similar functionality within a frequency band with distorted performances at frequencies other than the preset one.[19,26–30] Therefore, multiband metasurfaces are highly desirable to enrich the functional versatility of meta-devices, which is also beneficial for improving the information capacity. Intuitively, integrating two or more resonators into a supercell to form an interleaved metasurface or stacking multilayer metasurfaces is widely adopted to construct multiband metasurfaces,[20,26,31–35] which could lead to low efficiency due to the reduced number of the active resonators for each frequency or the increased fabrication complexities. Moreover, the period of the supercell might be greater than one-half wavelength at some frequency range, which could lead to higher order diffractions or lower imaging resolutions. Therefore, a multiband metasurface design strategy based on single-cell meta-atoms would be favored and more effective.

Very recently, a few multiband single-cell metasurface designs have been proposed, which include reflective dual-/tri/quad-band metallic meta-devices with the linear polarization and transmissive dual-/tri-band metallic meta-devices with the circular polarization.[17,30,36–41] Nevertheless, designing single-cell multiband metasurfaces at multiple closely separated frequencies remains challenging because of the mutual coupling among the constructing resonators due to the small footprint within the subwavelength meta-atom. In addition, most of the reported multiband metasurfaces consider only phase modulation.

R. Xie, Dr. G. Zhai, Dr. L. Li, Dr. J. Ding
State Key Laboratory of Precision Spectroscopy
Key Laboratory of Polar Materials and Devices
School of Physics and Electronic Sciences
East China Normal University
Shanghai 200241, China
E-mail: lli@lps.ecnu.edu.c; jding@ee.ecnu.edu.cn

D. Zhang, Dr. X. Wang
School of Information Science and Technology
ShanghaiTech University
Shanghai 201210, China

S. An, B. Zheng, Dr. H. Zhang
Department of Electrical and Computer Engineering
The University of Massachusetts Lowell
Lowell, MA 01854, USA

The ORCID identification number(s) for the author(s) of this article can be found under https://doi.org/10.1002/adpr.202100088.

DOI: 10.1002/adpr.202100088

However, simultaneous amplitude and phase modulations are highly desirable because more advanced wavefront manipulations can be enabled by introducing the independent amplitude modulations in addition to the phase modulations,[15,17,29,42] e.g., better holographic images and airy beams.

In this work, we demonstrate a high-efficiency tri-channel reflective metasurface with independent 2π phase modulation and 1-bit amplitude modulation at three distinct frequencies based on a novel single-cell tri-band meta-atom, which consists of a metallic top layer and a ground plane separated by a substrate spacer. The metallic top layer is perforated with two modified double-C-slot resonators (MDCSRs) and a slotted loop, where a double-C-shaped split-ring resonator (DCSRR) is located, thus, the meta-atom is composed of three alternately arranged metallic and slot resonators, each of which independently performs the complex-amplitude modulation at a corresponding frequency. By microtuning the geometrical parameters and orientation of each resonator appropriately, the single-cell meta-atom can reflect the circularly polarized incident wave to its copolarized component with independent complex-amplitude modulations at three frequencies. As a proof-of-concept demonstration, a tri-channel meta-device is designed, fabricated, and characterized, which could generate dual-vortex beams at f_1, quad-focus beams at f_2 and a hologram at f_3. The measured results have good agreements with the simulated ones, which validates the potential applications of the proposed tri-band single-cell metasurface, including ultra-compact image displays and high-density information storage.

2. Results and Discussion

The schematic illustration of the tri-channel metasurface is shown in **Figure 1**a. It can be observed from Figure 1a that a circularly polarized spherical wave is impinging on the metasurface by a horn antenna and the reflected copolarized field is recorded, realizing three different functionalities (i.e., a dual-vortex beam generator, a quad-focus metalens, and a meta-hologram at three preset frequencies f_1, f_2, and f_3, respectively). Especially, an anisotropic meta-atom is usually adopted for manipulating the phase shift of the circularly polarized wave by rotating the resonators, which is referred as geometric phase or Pancharatnam–Berry phase. While the meta-atom is rotated by an angle α, and illuminated by a left-handed/right-handed circularly polarized (LHCP/RHCP) plane wave propagating in $-z$ direction (i.e., $\vec{E}^i_{L/R} = (\hat{e}_x \pm j\hat{e}_y)A^i e^{jkz}e^{j\omega t}$), the reflected wave could be written in the following form[43]

$$\begin{aligned}\overrightarrow{E'}^r_{L/R} = & -\tfrac{1}{2}[(R_x e^{j\theta_x} - R_y e^{j\theta_y})(\hat{e}_x \mp j\hat{e}_y)e^{\pm 2j\alpha} \\ & + (R_x e^{j\theta_x} + R_y e^{j\theta_y})(\hat{e}_x \pm j\hat{e}_y)]A^i e^{-jkz}e^{j\omega t}\end{aligned} \quad (1)$$

where $\hat{e}_x$ and $\hat{e}_y$ are the unit vectors along the x- and y-directions in the Cartesian coordinates, respectively, A^i is the magnitude of the incident electric field along both the x- and y-directions, $k = 2\pi/\lambda$ is the wavevector, and $\omega = 2\pi c/\lambda$ is the angular frequency of the wave (c is the speed of light in vacuum, λ is the operation wavelength). In addition, R_x (R_y) and θ_x (θ_y) are the reflection coefficient and phase shift of the x-polarized (y-polarized) component of the reflected wave, respectively.

It is noted from Equation (1) that when illuminating an LHCP/RHCP light, the phase shift of the reflected cross-polarized component (i.e., RHCP/LHCP) is independent of the rotation angle α, whereas the phase shift of the copolarized component (i.e., LHCP/RHCP) is proportional to 2α. To obtain high efficiency and achieve geometric phase control for copolarized component of the circularly polarized incidence, the reflection coefficient and phase shift along x-/y-direction could be required as $R_x = R_y = 1$ and $\theta_x = \theta_y + \pi$, respectively. Then the reflected wave in Equation (1) becomes

$$\vec{E}'^r_{L/R} = (\hat{e}_x \mp j\hat{e}_y)e^{\pm 2j\alpha}RA^i e^{-jkz}e^{j\omega t} \quad (2)$$

Therefore, the reflected copolarized component has been delayed or advanced in phase by $\pm 2\alpha$ while the meta-atom

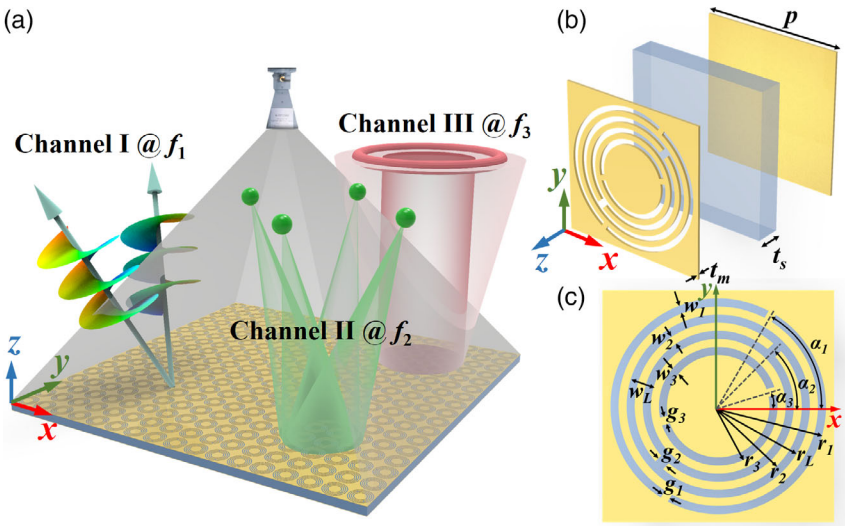

Figure 1. a) Schematic of the tri-channel meta-device. The structure is made of an array consisting of the proposed tri-band single-cell meta-atoms that produces dual-vortex beams, quad-focus beams and a holographic image of a ring at f_1, f_2, and f_3, respectively. b,c) The 3D and top views of the proposed tri-band single-cell meta-atom.

rotated by α, which indicates that continuous 2π phase modulation can be realized by rotating the meta-atom from 0 to π. Figure 1b,c shows the 3D view and the top view of the proposed tri-band single-cell meta-atom, which consists of a top patterned metallic layer, a dielectric spacer, and a ground plane. To achieve decoupling features among three frequencies, an annual loop is perforated to isolate the top metallic layer into three distinct regions (i.e., an outer metallic region, a ring hollow region, and an inner circular metallic region). The excited currents that reach the boundaries between regions would flow along the circular boundary, which performs as equivalently infinite and could considerably minimize the crosstalk between regions. Furthermore, the magnetic field coupled resonators (MACRs) could be etched in the outer and inner metallic parts, and the electric field coupled resonator (ELCR) could be placed in the middle hollow area. In this demonstrated illustration, the MDCSR and the DCSRR are adopted as MACR and ELCR, respectively. As shown in Figure 1c, the outer radius, width and incision gap width of the outer MDCSR/DCSRR/inner MDCSR are represented as $(r_1, w_1, g_1)/(r_2, w_2, g_2)/(r_3, w_3, g_3)$, respectively. The orientations of the three resonators are denoted as α_1, α_2, and α_3 with respect to the x-axis. In addition, the outer radius and width of the loop are labeled as (r_L, w_L). The thicknesses of the metal and substrate are denoted as t_m and t_s, respectively.

In addition, the metal and substrate are selected to be the copper (conductivity $= 5.96 \times 10^7$ S m^{-1}) and the polytetrafluoroethylene material (product name: F4B, dielectric constant of $\varepsilon_r = 2.2$, loss tangent of $\tan\delta = 0.001$) with $t_m = 0.035$ mm and $t_s = 3$ mm, respectively. The periodicity of the meta-atom denoted as p is chosen to be 8.4 mm, and the annual loop with $r_L = 3.65$ mm and $w_L = 0.7$ mm are fixed in the following design. **Figure 2**a–c shows the top views of the three resonators, i.e., the outer MDCSR, middle DCSRR, and inner MDCSR, whose dimensional parameters are $(r_1, w_1, g_1) = (4.1, 0.2, 0.3)$, $(r_2, w_2, g_2) = (3.4, 0.2, 0.4)$, and $(r_3, w_3, g_3) = (2.75, 0.2, 0.2)$ (unit: mm), respectively. The meta-atoms are simulated by the fullwave simulator CST Microwave Studio, where the periodic boundary conditions in x-/y-directions and plane wave excitation along $-z$-direction are applied. Figure 2e–g shows the reflection amplitudes of the three resonators, where the orientation angle of each resonator (i.e., α_1, α_2, and α_3) is varied with a step interval of $\pi/8$ under a RHCP incidence. It can be observed from Figure 2e that the reflection amplitude reaches a maximum of 0.93 at $f_1 = 9.5$ GHz while maintaining low values in the rest of frequencies. Similarly, Figure 2f,g shows reflection amplitude maxima occurred around $f_2 = 11.5$ GHz and $f_3 = 15$ GHz, which indicates that each resonator corresponds to one frequency band. Furthermore, it is worth mentioning that the period of the meta-atom is smaller than the half wavelength at the highest operation frequency (i.e., $p < c/(2f_3)$). When the three resonators (i.e., outer MDCSR, middle DCSRR, and inner MDCSR) are appropriately arranged to construct the proposed tri-band single-cell meta-atom, as shown in Figure 2d, the reflection amplitudes are simultaneously maximized at the three frequency bands of the three resonators, as shown in Figure 2h. The decoupled feature leads to a straightforward design for regulating the operation frequencies by independently adjusting the sizes of these three resonators.

Furthermore, when individually rotating each of the three resonators with a step interval of $\pi/8$, the reflection copolarized amplitudes and phase shifts under a RHCP incidence are shown in Figure 2i–k,m–o, respectively, where the gray-shadowed areas represent the amplitude of >0.8 and phase with a uniform $\pi/4$ shift. Specifically, it can be seen from Figure 2i,m that while rotating α_1 with fixed α_2 and α_3, the reflection amplitude holds a relatively high level at all three frequencies, and the phase shows uniform variation of $2\alpha_1$ at the range of 9–10 GHz. Moreover, the negligible phase variations can be observed at 11–15.5 GHz. Similar conclusions can be drawn from Figure 2j,n for 11.5 GHz and from Figure 2k,o for 15 GHz, indicating the completely independent phase control at each operating frequency, as well as the low cross-talks among three resonators.

More interestingly, benefiting from the decoupling among the three resonators, the 1-bit amplitude modulation at each frequency could be realized by simply removing the corresponding resonator or replacing the resonator for a nonresonant structure. As a demonstration in this work, the replacing method is used. In other words, when a meta-atom with zero reflection amplitude is required in a metasurface array, the corresponding DCSRR (MDCSR) is replaced by a metallic ring (a ring slot) as shown in Figure S1, Supporting Information, where the phase and amplitude responses are detailed in the Supporting Information. Therefore, the independent 1-bit amplitude modulations at three frequencies can be achieved, which can be denoted as on–off states.

As discussed in Equation (2), the high efficiency with copolarized conversion is obtained while the reflection coefficients of the metasurface satisfies the criterion of $R_x = R_y = 1$ and $\theta_x = \theta_y + \pi$. To verify this condition, the x- and y-polarized waves are normally incident on the tri-band meta-atom, and the copolarized reflection amplitude and phase responses are recorded in Figure 2l,p, respectively, which are represented as $|\vec{E}^r_{xx}|$, $|\vec{E}^r_{yy}|$, $\angle\vec{E}^r_{xx}$ and $\angle\vec{E}^r_{yy}$. Figure 2l shows that the two orthogonally polarized reflection amplitudes are almost equal in the proposed range of 7–19 GHz, where a little difference between x- and y-component occurs due to resonance-induced loss. In addition, the phase differences between $\angle\vec{E}^r_{xx}$ and $\angle\vec{E}^r_{yy}$ are around π at 9.5, 11.5, and 15 GHz, which satisfies the ideal condition, as shown in Equation (2).

To validate the performance of the proposed tri-band single-cell meta-atom, a tri-channel meta-device is numerically and experimentally demonstrated to showcase three different functionalities at three frequencies. More specifically, the meta-device realizes a dual-vortex beam generator, a quad-focus metalens, and a meta-hologram at 9.5, 11.5, and 15 GHz, respectively.

The fundamental principle for multibeam radiation relies on the superposition of several basic complexed amplitudes. Thus, the complex-valued amplitude distribution (E) of a multibeam metasurface is formulated as

$$\begin{aligned} E(x,y,f_i) &= a(x,y,f_i)e^{j\theta(x,y,f_i)} = \sum_{n=1}^{N} E_n(x,y,f_i) \\ &= \sum_{n=1}^{N} a_n(x,y,f_i)e^{j\theta_n(x,y,f_i)} \end{aligned} \tag{3}$$

where E_n is the complex-valued amplitude of the nth beam, a and θ (a_n and θ_n) represent the amplitude and phase at the position

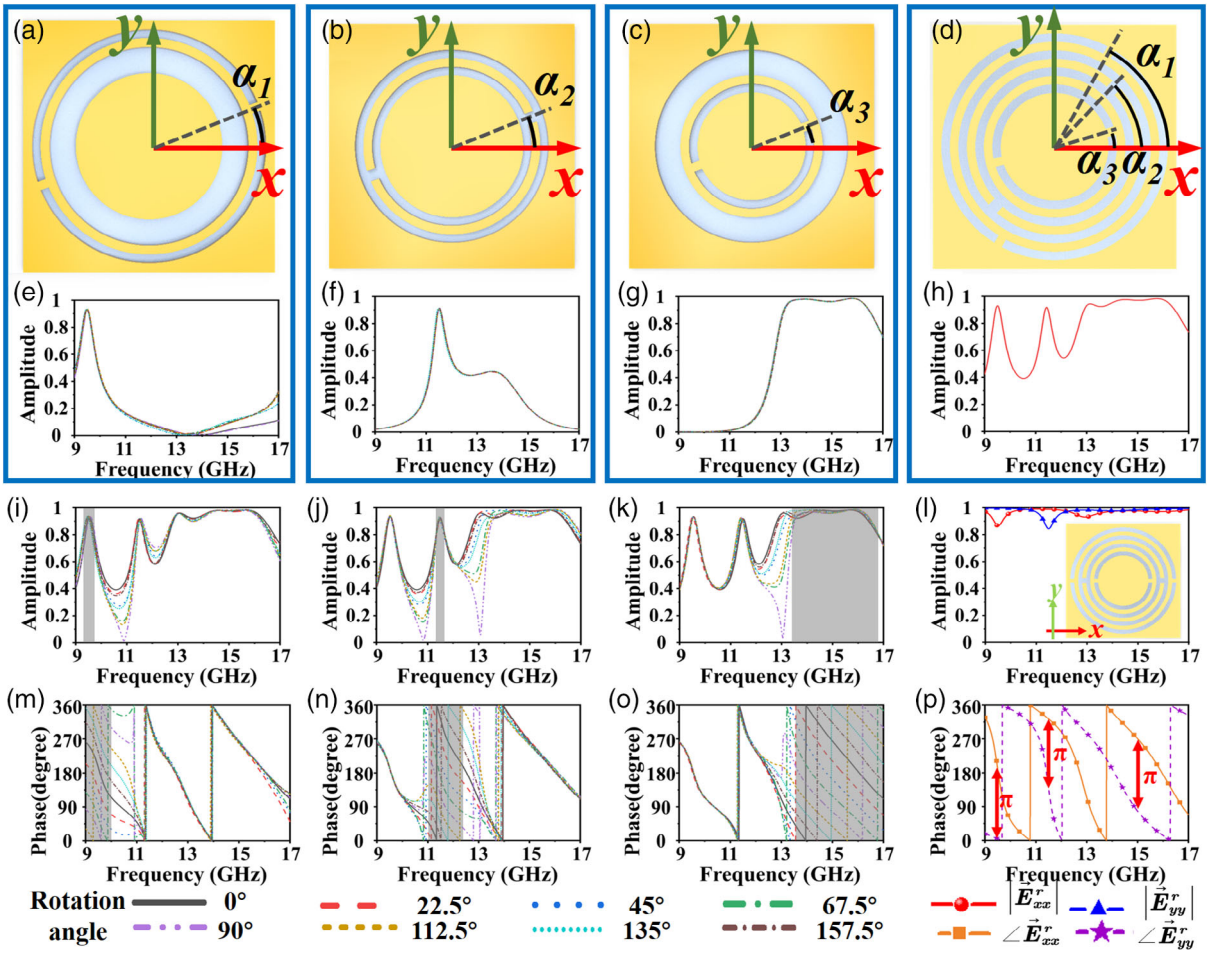

Figure 2. a–c) The top views of the three resonators operating at 9.5, 11.5, and 15 GHz, where the outer MDCSR, middle DCSRR, and inner MDCSR, respectively, are added to each of the three region. d) The top view of the proposed tri-band single-cell meta-atom combined by the three resonators in (a)–(c). e–g) The simulation reflection copolarized amplitudes of the single-band meta-atoms shown in (a)–(c) while rotating every resonator from 0 to $7\pi/8$ with a step interval of $\pi/8$ under a RHCP incidence. h) The simulation reflection copolarized amplitude of the tri-band meta-atom shown in (d). i–k) The simulation reflection copolarized amplitudes for the tri-band single-cell meta-atom by varying i) α_1, j) α_2, and k) α_3. m–o) The simulated reflection phase shifts for the tri-band single-cell meta-atom by varying m) α_1, n) α_2, and (o) α_3. Gray-shaded areas indicate amplitude of >0.8 or uniform phase shift. l,p) The simulation reflection copolarized amplitude and phase shift under *x*- and *y*-polarized illumination.

(x, y), which could be extracted from the complex-valued amplitude of E (E_n). In addition, N is the number of the EM beams at the ith operation frequency of f_i. The synthetic multibeam radiation can be arbitrarily engineered according to predefined composite functions. Here, to facilitate versatile functions, multibeam scatterings carrying different topological charges of orbital angular momentum (OAM), as well as converging energy at a preset distance are explored as the first function for channel 1. The vortex beam contains the helical phase front along azimuthal direction ($\theta^1(x, y, l) = l \cdot \arctan(y/x)$, where l is the topological charge). Furthermore, each beam is designed to focus energy on a preset distance (F) from the metasurface, which requires a parabola phase distribution along radial direction ($\theta^2(x, y, f, F) = 2\pi f/c\sqrt{x^2 + y^2 + F^2}$). Finally, a beam directed in an arbitrary orientation demands an uniform gradient phase distribution, which could be described as

$$\theta^3(x, y, \theta, \varphi) = \mathrm{Sign}(\hat{e}_r \cdot \hat{e}_\varphi) \cdot 2\pi f/c \cdot |\cos\varphi \cdot x + \sin\varphi \cdot y| \cdot \sin\theta \quad (4)$$

where Sign represents the signum function, φ and θ are the azimuth and elevation angles of the beam radiation direction, respectively. In addition, $\hat{e}_r$ *and* $\hat{e}_\varphi$ are the unit vectors of (x, y) and $\vec{\varphi}$, respectively. Therefore, the complex-amplitude distribution of a multivortex beam generator could be summarized as the following

$$E(x, y, f_i) = a(x, y, f_i) e^{j\theta(x, y, f_i)} = \sum_{n=1}^{N} a_n(x, y, f_i) e^{j\left[\theta_n^1(x, y, l_n) + \theta_n^2(x, y, f_i, F_i) + \theta_n^3(x, y, f_i, \theta_n, \varphi_n)\right]} \quad (5)$$

In this example, we consider a dual-vortex beam generator, which obtains the same focal length ($F_1 = F_2 = 200$ mm) but

different topological charges ($l_1 = +1$, $l_2 = -1$) and radiation directions ((θ, φ) = (15°,0°)/(15°,180°)) at $f_1 = 9.5$ GHz, as shown in **Figure 3**a. Because the dual-vortex beams have the same elevation angle, the coefficients of the two basic beams are determined to be the same value (i.e., $a_1 = a_2$) for obtaining equal radiation powers.[44] Figure 3b,c shows the digitized 1-bit amplitude and phase distributions (i.e., a and θ) calculated by Equation (5) at 9.5 GHz, where the metasurface is composed of 31 × 31 meta-atoms, covering an area of 260.4 × 260.4 mm^2.

Next, we choose to implement the multi-focus metalens for channel 2. The phase profile required for a single-focus metalens could be obtained based on the Fermat's theorem and expressed as $\theta(x, y, f) = 2\pi f/c \cdot (\sqrt{(x-x_1)^2 + (y-y_1)^2 + z_1^2} - z_1)$, where ($x_1$, y_1, z_1) is the coordinates of a focal spot. Thus, the complex-amplitude of a multifocus beam is given by

$$E(x, y, f_i) = a(x, y, f_i) e^{j\theta(x,y,f_i)} = \sum_{n=1}^{N} a_n(x, y, f_i) e^{j2\pi f_i/c \cdot (\sqrt{(x-x_n)^2 + (y-y_n)^2 + z_n^2} - z_n)} \quad (6)$$

where (x_n, y_n, z_n) is the coordinates of the nth focal spot. The quad-focus metalens is then calculated for $f_2 = 11.5$ GHz, with the focal spots located at I(50, 50, 200)/II(−50, 50, 200)/III(−50, −50, 200)/IV(50, −50, 200), as shown in Figure 3f. The digitized amplitude and phase distributions are shown in Figure 3g,h, respectively.

Finally, a meta-hologram is studied for channel 3. Holography-based techniques are intended for modulating the amplitude and phase of spatial fields, which have been utilized in 3D holographic displays and data storage. The complex-amplitude profile for the hologram could be calculated by Rayleigh–Sommerfeld diffraction integral, and optimized with the classical Gerchberg–Saxton (GS) algorithm, which is expressed as

$$E(x, y, f_i) = a(x, y, f_i) e^{j\theta(x,y,f_i)} = \iint_{S'} E'(x', y', f_i) \frac{f_i d}{ic} \cdot \frac{e^{-j2\pi f/c|\boldsymbol{r}|}}{|\boldsymbol{r}|^2} ds' \quad (7)$$

where E and E' are the complex-valued amplitudes on the meta-hologram plane and the image plane, respectively, d denotes the distance between the two planes, $\boldsymbol{r}$ is the vector of arbitrary two points on the two planes, and S' is the image region. As a proof-of-concept demonstration, the target image of a ring is chosen to be reconstructed by the meta-hologram at $f_3 = 15$ GHz, as shown in Figure 3k. The calculated amplitude and phase distributions for the eventually optimized result are shown in Figure 3l,m, respectively. Furthermore, it is noted that the three channels are calculated while illuminated by a plane wave. However, the metasurface is illuminated by a spherical wave emitting from a horn antenna in the experiment. Therefore, the phase compensation for transferring the spherical incident wave into the plane wave is added on the designed tri-channel metasurface, which could be described as

$$\theta_{com}(x, y, f_i, L) = 2\pi f_i/c(\sqrt{x^2 + y^2 + L^2} - L) \quad (8)$$

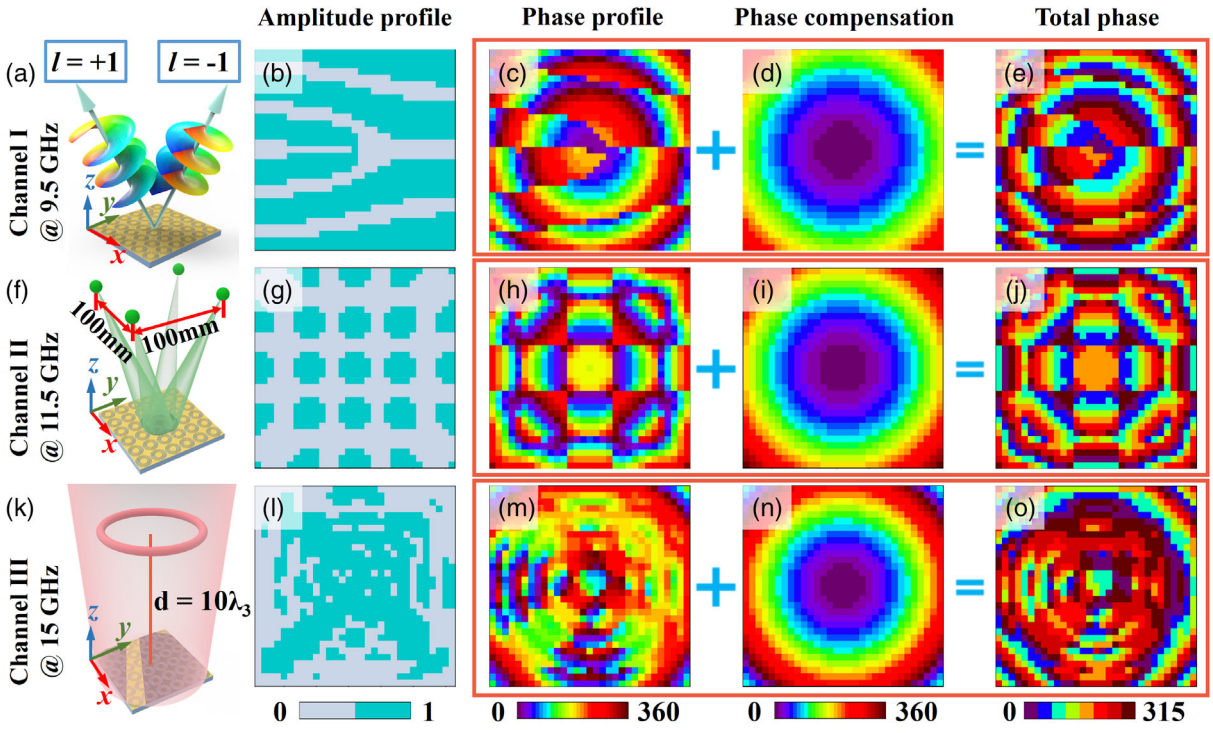

Figure 3. a,f,k) Schematic illustration of three channels for 9.5, 11.5, and 15 GHz, where the a) dual-vortex beam generator, f) quad-focus metalens, and k) meta-hologram are achieved at each channel respectively. b,g,l) The digitized amplitude profiles for three channels at b) 9.5, g) 11.5, and l) 15 GHz. c,h, m) The phase profiles for three channels at c) 9.5, h) 11.5, and m) 15 GHz. d,i,n) The phase compensations for transferring the spherical incident wave into the plane wave on the metasurface at d) 9.5, i) 11.5, and n) 15 GHz. e,j,o) The digitized total phases at e) 9.5, j) 11.5, and o) 15 GHz.

where (x, y) denotes the position of each meta-atom and L denotes the distance between the transmitting antenna and the metasurface. Figure 3d,i,n, shows the compensation phase for 9.5, 11.5, and 15 GHz while $L = 600$ mm, respectively. The digitized total phases for the designed tri-channel meta-device are shown in Figure 3e,j,o by superimposing the original phase and the compensation phase.

The designed tri-channel metasurface is verified by full-wave simulation. In the simulations, a RHCP horn is used as the transmitter, and the reflected copolarized electric fields are recorded. **Figure 4**a shows the simulated intensity of RHCP field on the XZ plane at 9.5 GHz, where the reflected wave splitting into two beams with $(\theta, \varphi) = (15°,0°)/(15°,180°)$ could be clearly noticed. Moreover, the energy of both beams is converged at the preset distance of 200 mm. The normalized intensity and phase distributions at the focal plane are shown in Figure 4b,c, respectively, where the intensity nulls and spiral phase patterns at the corresponding positions could be observed clearly. Moreover, the number of the spiral arms and the rotation direction of the phase distribution indicate the topological charges of $l = +1$ and $l = -1$ in the region I and region II, respectively, which satisfies the design goals. Figure 4d,e shows the simulated intensity distributions on the XZ plane of $y = 50$ mm and the XY plane of $z = 200$ mm at 11.5 GHz. Figure 4d,e shows that four focal spots occur at I(50, 50, 200)/II(−50, 50, 200)/III(−50, −50, 200)/IV(50, −50, 200) simultaneously. Furthermore, Figure 4f shows the simulated result for meta-hologram at 15 GHz, which displays a pattern of a ring clearly.

Next, the tri-channel metasurface based on the tri-band single-cell meta-atom is fabricated and measured. **Figure 5**a shows the top view of the fabricated sample. Figure 5b shows the schematic of the measurement system, where a circularly polarized horn antenna (LB-SJ-60180-P03, 6–18 GHz) is used as a transmitter and located at a fix distance of 600 mm away from the meta-device. In addition, two type of linearly polarized waveguide antenna (90WCAS, 8.2-12.4 GHz; HD-140VNAWKS, 11.9–18 GHz) are selected as receivers because their small size could effectively reduce blocking effect. In the measurement, the receiver would detect both x- and y-polarized electric fields on the target plane, which are then converted to the circularly polarized fields based on the transformation relationship of $\vec{E}_{L/R} = \vec{E}_x \mp j\vec{E}_y$. Figure 5c,d shows the measured intensity distributions on the XZ plane with $y = 0$ and the XY plane with $z = 200$ mm at 9.5 GHz, respectively, where the reflected beam splits into two directions and focused on the predesigned distance of 200 mm. Furthermore, the intensity nulls at two focal spots are shown in Figure 5d, where the spiral phase distributions are obtained for both nulls and denote the different OAM modes of $+1/-1$ in region I/II, respectively, as shown in the insets of Figure 5d. Furthermore, the coordinates of the center point of the doughnuts are (−54,0,200)/(54,0,200) (unit: mm), which indicates that the directed angles of the two OAM beams are 15.3°. Moreover, the mode purities of the OAM beams are evaluated to characterize the efficiency of the dual-vortex beam generator, which is based on spectral analysis of Fourier transform.[45,46] As shown in Figure 5e, the

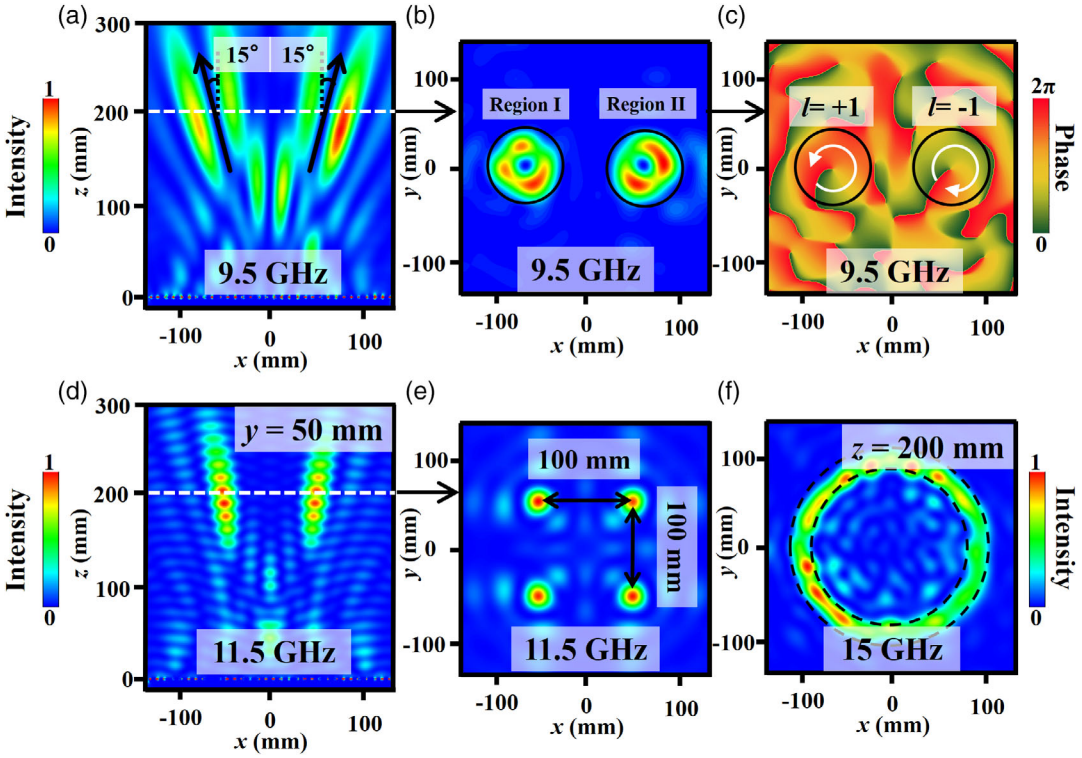

Figure 4. a) The simulated intensity on the XZ plane at 9.5 GHz. b,c) The simulated intensity and phase distributions on the XY plane (i.e., $z = 200$ mm) at 9.5 GHz. d,e) The simulated intensity distributions on d) the XZ plane with $y = 50$ mm and e) the XY plane with $z = 200$ mm at 11.5 GHz. f) The simulated intensity distribution on the XY plane with $z = 200$ mm at 15 GHz.

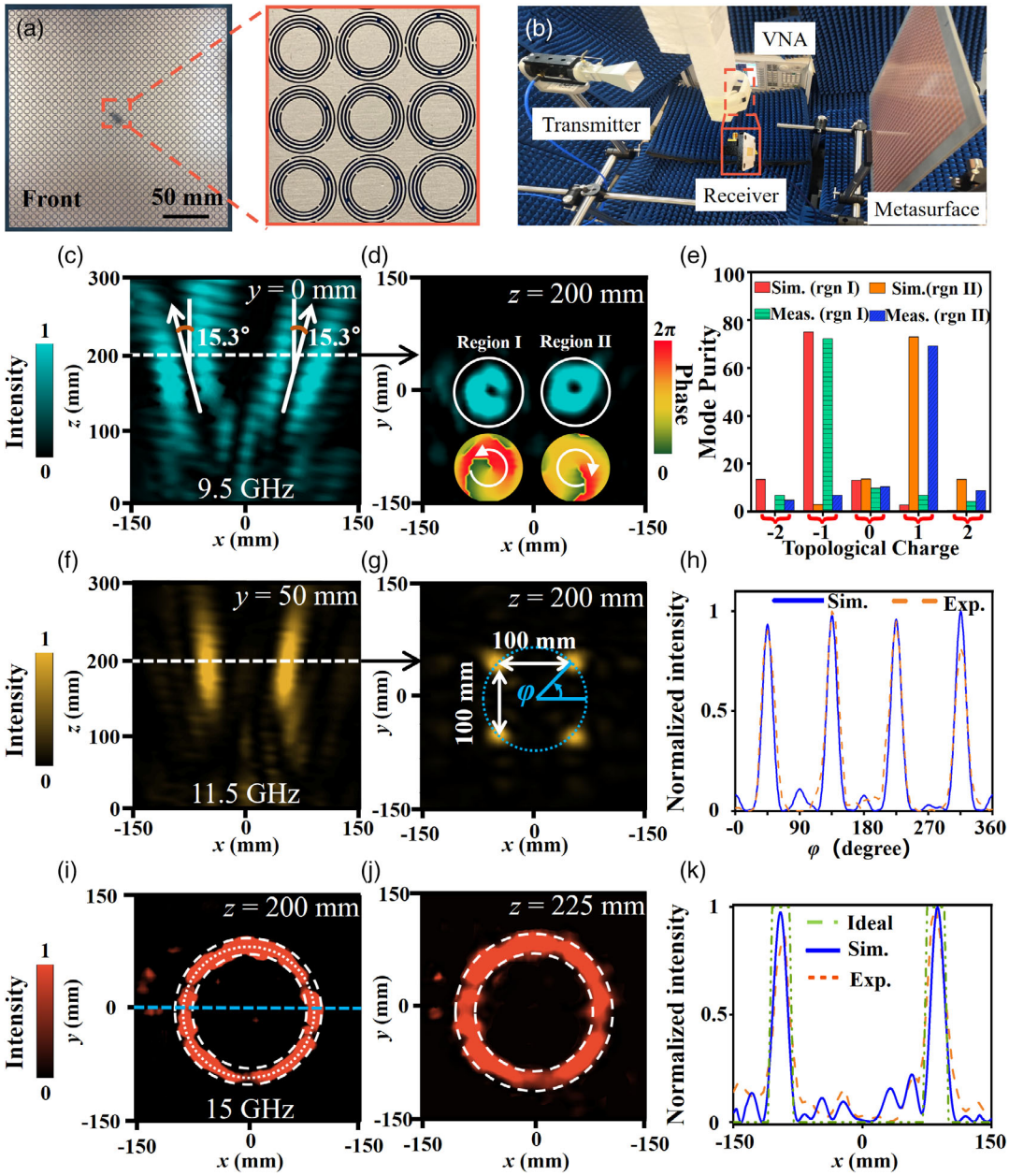

Figure 5. a) The fabricated sample of the proposed tri-channel metasurface. b) Schematic of the experimental setup. c,d) The measured intensity distributions on c) the *XZ* plane with $y = 0$ and d) the *XY* plane with $z = 200$ mm at 9.5 GHz, where insets show the phase distributions in region I/II. e) The simulated and measured mode purity of the OAMs for regions I and II at 9.5 GHz. f,g) The measured intensity distributions on f) the *XZ* plane with $y = 50$ mm and g) the *XY* plane with $z = 200$ mm. h) Normalized intensity profile along blue circular dashed line stroked in (g). i,j) The measured intensity distributions on the *XY* plane with i) $z = 200$ mm and j) $z = 225$ mm at 15 GHz. k) Normalized intensity profile along blue dashed line stroked in (i). The scanning step is 5 mm.

simulated and measured dominant modes in region I (region II) are both +1 (−1) with a purity of 75% and 73% (72% and 69%), respectively, validating that high mode purities can be achieved in channel 1.

Figure 5f,g shows the intensity distributions for channel 2 on the *XZ* plane with $y = 50$ mm and the *XY* plane with $z = 200$ mm at 11.5 GHz, respectively, where the four focal spots could be clearly seen at the designed positions, and the distance between two adjacent focal spots is close to 100 mm. To quantitatively characterize the impact of the quad-focus metalens, the intensity profiles as a function of azimuth φ, which are along the blue circular dashed line with the radius of 70.7 mm in Figure 5g, are shown in Figure 5h. Four peaks of the intensity occur at $\varphi = 45°/135°/225°/315°$ in both simulation and experiment results, indicating good focusing performance at the channel 2. Finally, The measured intensity distributions for channel 3 on the *XY* planes

of $z = 200/225$ mm at 15 GHz are plotted in Figure 5i,j, respectively. The patterns of a ring are reconstructed with good image qualities on the observation planes. In addition, Figure 5k plots the intensity distributions along the dashed line from left to right in Figure 4f for the simulation and Figure 5i for the experiment. It can be observed from Figure 5k that the simulated result agrees well with the measured ones, conformal to the ideal case as well.

Furthermore, an additional experimental setup is carried out for calculating the reflection efficiency, where the meta-device is replaced by the metal plate with the same area. The reflection efficiency is defined as the ratio of the total intensity with meta-device to that with the metal plate within the identical detection region. Herein, the reflection intensity on the *XY* plane is detected with an area of $300 \times 300\ \text{mm}^2$ at a distance of $z = 200$ mm. And the reflection efficiencies are evaluated to be 73.02%, 72.81%, and 78.96% for 9.5, 11.5, and 15 GHz, respectively. The blockage of the receiving antenna and the measurement region would affect the efficiency.

3. Conclusion

In summary, we demonstrate a novel design approach for achieving high-efficiency tri-band single-cell metasurface featuring complex-amplitude modulations at three independent frequencies. The tri-band single-cell meta-atom consists of a perforated metallic top layer and a ground plane separated by a substrate spacer, where the top layer composing of three resonators (i.e., two MDCSRs and a DCSRR). The full 2π phase modulations at three frequencies could be realized by simply varying the orientations of the corresponding resonators, and the 1-bit amplitude control could be achieved by choosing the on–off state of the corresponding resonators. As a proof-of-concept demonstration, a tri-channel metasurface based on the tri-band metasurface are designed, fabricated, and measured, realizing a dual-vortex beam generator, a quad-focus metalens and a meta-hologram at three arbitrarily chosen frequencies. Specially, the dual-vortex beam generator reflects incident wave toward $(\theta,\ \varphi) = (15^\circ,0^\circ)/(15^\circ,180^\circ)$ with two different topological charges of ± 1 at 9.5 GHz. In addition, a quad-focus metalens converges the reflection wave at four preset spots at 11.5 GHz. Furthermore, the metasurface displays a ring image at 15 GHz. With the inherent advantages such as compactness, flexible design for polarization, and easy fabrication, the tri-band single-cell metasurface has great potential for practical applications such as display, communication system, and many other related fields.

Supporting Information

Supporting Information is available from the Wiley Online Library or from the author.

Acknowledgements

This work was supported by the National Key R&D Program of China 2019YFA0705000, Shanghai Pujiang Program (grant 18PJ1403200), Fundamental Research Funds for Central Universities, and a research grant from the U.S. National Science Foundation (1661749).

Conflict of Interest

The authors declare no conflict of interest.

Data Availability Statement

Research data are not shared.

Keywords

complex-amplitude modulation, multichannels, single-cell meta-atoms, tri-band metasurfaces

Received: March 22, 2021
Revised: May 31, 2021
Published online: August 5, 2021

[1] N. Yu, P. Genevet, M. A. Kats, F. Aieta, J.-P. Tetienne, F. Capasso, Z. Gaburro, *Science* **2011**, *334*, 333.
[2] X. Ni, N. K. Emani, A. V. Kildishev, A. Boltasseva, V. M. Shalaev, *Science* **2012**, *335*, 427.
[3] A. V. Kildishev, A. Boltasseva, V. M. Shalaev, *Science* **2013**, *339*, 1232009.
[4] E. Karimi, S. A. Schulz, I. De Leon, H. Qassim, J. Upham, R. W. Boyd, *Light: Sci. Appl.* **2014**, *3*, e167.
[5] K. Huang, H. Liu, F. J. Garcia-Vidal, M. Hong, B. Luk'yanchuk, J. Teng, C.-W. Qiu, *Nat. Commun.* **2015**, *6*, 7059.
[6] K. E. Chong, I. Staude, A. James, J. Dominguez, S. Liu, S. Campione, G. S. Subramania, T. S. Luk, M. Decker, D. N. Neshev, I. Brener, Y. S. Kivshar, *Nano Lett.* **2015**, *15*, 5369.
[7] F. Yue, C. Zhang, X.-F. Zang, D. Wen, B. D. Gerardot, S. Zhang, X. Chen, *Light: Sci. Appl.* **2018**, *7*, 17129.
[8] M. Khorasaninejad, W. T. Chen, R. C. Devlin, J. Oh, A. Y. Zhu, F. Capasso, *Science* **2016**, *352*, 1190.
[9] M. Khorasaninejad, A. Y. Zhu, C. Roques-Carmes, W. T. Chen, J. Oh, I. Mishra, R. C. Devlin, F. Capasso, *Nano Lett.* **2016**, *16*, 7229.
[10] X. Ding, F. Monticone, K. Zhang, L. Zhang, D. Gao, S. N. Burokur, A. de Lustrac, Q. Wu, C.-W. Qiu, A. Alù, *Adv. Mater.* **2015**, *27*, 1195.
[11] P.-Y. Chen, A. Alù, *Phys. Rev. B* **2011**, *84*, 205110.
[12] X. Ni, Z. J. Wong, M. Mrejen, Y. Wang, X. Zhang, *Science* **2015**, *349*, 1310.
[13] A. Arbabi, Y. Horie, M. Bagheri, A. Faraon, *Nat. Nanotechnol.* **2015**, *10*, 937.
[14] J. Zeng, L. Li, X. Yang, J. Gao, *Nano Lett.* **2016**, *16*, 3101.
[15] X. Ni, A. V. Kildishev, V. M. Shalaev, *Nat. Commun.* **2013**, *4*, 2807.
[16] L. Huang, X. Chen, H. Mühlenbernd, H. Zhang, S. Chen, B. Bai, Q. Tan, G. Jin, K.-W. Cheah, C.-W. Qiu, J. Li, T. Zentgraf, S. Zhang, *Nat. Commun.* **2013**, *4*, 2808.
[17] R. Xie, M. Xin, S. Chen, D. Zhang, X. Wang, G. Zhai, J. Gao, S. An, B. Zheng, H. Zhang, J. Ding, *Adv. Opt. Mater.* **2020**, *8*, 2000919.
[18] D. Wen, F. Yue, G. Li, G. Zheng, K. Chan, S. Chen, M. Chen, K. F. Li, P. W. H. Wong, K. W. Cheah, E. Yue Bun Pun, S. Zhang, X. Chen, *Nat. Commun.* **2015**, *6*, 8241.
[19] Y. Montelongo, J. O. Tenorio-Pearl, C. Williams, S. Zhang, W. I. Milne, T. D. Wilkinson, *Proc. Natl. Acad. Sci.* **2014**, *111*, 12679.
[20] Y. Hu, X. Luo, Y. Chen, Q. Liu, X. Li, Y. Wang, N. Liu, H. Duan, *Light: Sci. Appl.* **2019**, *8*, 86.
[21] J. Li, Y. Wang, C. Chen, R. Fu, Z. Zhou, Z. Li, G. Zheng, S. Yu, C. Qiu, S. Zhang, *Adv. Mater.* **2021**, *33*, 2007507.
[22] Q. Dai, Z. Guan, S. Chang, L. Deng, J. Tao, Z. Li, Z. Li, S. Yu, G. Zheng, S. Zhang, *Adv. Funct. Mater.* **2020**, *30*, 2003990.

[23] Z. Li, C. Chen, Z. Guan, J. Tao, S. Chang, Q. Dai, Y. Xiao, Y. Cui, Y. Wang, S. Yu, G. Zheng, S. Zhang, *Laser Photonics Rev.* **2020**, *14*, 2000032.
[24] S. Linden, F. B. P. Niesler, J. Förstner, Y. Grynko, T. Meier, M. Wegener, *Phys. Rev. Lett.* **2012**, *109*, 015502.
[25] N. Meinzer, W. L. Barnes, I. R. Hooper, *Nat. Photonics* **2014**, *8*, 889.
[26] F. Aieta, M. A. Kats, P. Genevet, F. Capasso, *Science* **2015**, *347*, 1342.
[27] B. Wang, F. Dong, Q.-T. Li, D. Yang, C. Sun, J. Chen, Z. Song, L. Xu, W. Chu, Y.-F. Xiao, Q. Gong, Y. Li, *Nano Lett.* **2016**, *16*, 5235.
[28] E. Arbabi, A. Arbabi, S. M. Kamali, Y. Horie, A. Faraon, *Optica* **2016**, *3*, 628.
[29] J. Ding, S. An, B. Zheng, H. Zhang, *Adv. Opt. Mater.* **2017**, *5*, 1700079.
[30] R. Xie, G. Zhai, X. Wang, D. Zhang, L. Si, H. Zhang, J. Ding, *Adv. Opt. Mater.* **2019**, *7*, 1900594.
[31] D. Wen, J. J. Cadusch, J. Meng, K. B. Crozier, *Adv. Funct. Mater.* **2020**, *30*, 1906415.
[32] Q. Wei, B. Sain, Y. Wang, B. Reineke, X. Li, L. Huang, T. Zentgraf, *Nano Lett.* **2019**, *19*, 8964.
[33] X. Luo, Y. Hu, X. Li, Y. Jiang, Y. Wang, P. Dai, Q. Liu, Z. Shu, H. Duan, *Adv. Opt. Mater.* **2020**, *8*, 1902020.
[34] F. Zhang, M. Pu, P. Gao, J. Jin, X. Li, Y. Guo, X. Ma, J. Luo, H. Yu, X. Luo, *Adv. Sci.* **2020**, *7*, 1903156.
[35] Y. Bao, Y. Yu, H. Xu, C. Guo, J. Li, S. Sun, Z.-K. Zhou, C.-W. Qiu, X.-H. Wang, *Light: Sci. Appl.* **2019**, *8*, 95.
[36] M. Xin, R. Xie, G. Zhai, J. Gao, D. Zhang, X. Wang, S. An, B. Zheng, H. Zhang, J. Ding, *Opt. Express* **2020**, *28*, 17374.
[37] H. Hasani, M. Tamagnone, S. Capdevila, C. F. Moldovan, P. Maoddi, A. M. Ionescu, C. Peixeiro, J. R. Mosig, A. K. Skrivervik, J. Perruisseau-Carrier, *IEEE Trans. Terahertz Sci. Technol.* **2016**, *6*, 268.
[38] H. Hasani, C. Peixeiro, A. K. Skrivervik, J. Perruisseau-Carrier, *IEEE Trans. Antennas Propag.* **2015**, *63*, 5522.
[39] G. D. Bai, Q. Ma, S. Iqbal, L. Bao, H. B. Jing, L. Zhang, H. T. Wu, R. Y. Wu, H. C. Zhang, C. Yang, T. J. Cui, *Adv. Opt. Mater.* **2018**, *6*, 1800657.
[40] R. Xie, G. Zhai, J. Gao, D. Zhang, X. Wang, S. An, B. Zheng, H. Zhang, J. Ding, *Adv. Theory Simul.* **2020**, *3*, 2000099.
[41] T. Wang, G. Zhai, R. Xie, S. Zhu, J. Gao, S. An, B. Zheng, H. Li, Y. Liu, H. Zhang, J. Ding, *Adv. Theory Simul.* **2019**, *2*, 1900071.
[42] L. Liu, X. Zhang, M. Kenney, X. Su, N. Xu, C. Ouyang, Y. Shi, J. Han, W. Zhang, S. Zhang, *Adv. Mater.* **2014**, *26*, 5031.
[43] J. Huang, R. J. Pogorzelski, *IEEE Trans. Antennas Propag.* **1998**, *46*, 650.
[44] H. Rajabalipanah, A. Abdolali, J. Shabanpour, A. Momeni, A. Cheldavi, *ACS Omega* **2019**, *4*, 14340.
[45] B. Jack, M. J. Padgett, S. Franke-Arnold, *New J. Phys.* **2008**, *10*, 103013.
[46] M. J. Strain, X. Cai, J. Wang, J. Zhu, D. B. Phillips, L. Chen, M. Lopez-Garcia, J. L. O'Brien, M. G. Thompson, M. Sorel, S. Yu, *Nat. Commun.* **2014**, *5*, 4856.